Hindawi
International Journal of Aerospace Engineering
Volume 2022, Article ID 5257939, 16 pages
https://doi.org/10.1155/2022/5257939

Research Article

Reconstruction of Wing Structure Deformation Based on Particle Swarm Optimization Ridge Regression

Xinyi Wu, Zhiwei Xu, and Jie Zeng

State Key Laboratory of Mechanics and Control of Mechanical Structures, Nanjing University of Aeronautics and Astronautics, Nanjing 210016, China

Correspondence should be addressed to Xinyi Wu; wuxinyi@nuaa.edu.cn

Received 20 August 2021; Revised 17 February 2022; Accepted 22 March 2022; Published 12 April 2022

Academic Editor: Adel Ghenaiet

In this paper, a typical airfoil aluminum plate structure is taken as the research object. A structural deformation monitoring and reconstruction method, PSO-RR (particle swarm optimization-ridge regression) algorithm, is proposed. A variety of different complex load cases are applied to the airfoil structure, and the strain values at some specific positions of the structure are collected. The ridge regression algorithm is used to construct the theoretical model of the relationship between the strain and structural deformation. Then, the structural displacements with different load cases are monitored and reconstructed. To improve the precision, the PSO algorithm is used to optimize the ridge regression parameters and comparative analysis is carried out with the typical structural deformation reconstruction algorithm, such as the KO theoretical method. Results show that the PSO-RR predicts the deformation of complex wing structures under different kinds of complex load cases accurately. This method, which has high precision, does not depend on the specific structures and load cases.

1. Introduction

The aircraft is subjected to high aerodynamic loads during flight. The bending deformation of the wing makes it easy to produce stress concentration in some parts (such as the root of the wing). The long-time fatigue stress may endanger flight safety. Especially, for the next-generation of flexible variant aircraft, which has been studied deeply for a long time, its wing deformation scale is larger, and the deformation modes are very different from the traditional aircraft. It is difficult to get the real-time deformation data and transform the strain data into displacements. In addition, the aerodynamic loads of the wing are complex and change in real-time during flight. The real-time wing deformation during flight can be used for shape control and structural failure monitoring and prediction; it is a key issue that must be resolved [1]. Therefore, studies on wing deformation monitoring and reconstruction under complex load conditions are significant.

Currently, the wing deformation measurement technology can be divided into two types, contact and noncontact. The noncontact measurement method mainly focuses on image capture, laser scanning, and tracking [2, 3]. The target point needs to be located by light, which is greatly affected by environmental factors and difficult to calibrate and install. Therefore, contact measurement technology has been continuously developed and applied [4]. Strain, pressures, velocities, and other related information are obtained through sensors arranged on the surface or inside of the wing. Then, the status of the wing can be monitored. The wing strain information can be equivalently converted into structural deformation. The deformation reconstruction methods based on strain monitoring are mainly divided into the following types. Hauge and Foss [5] proposed modal transformation algorithms for the first time, which used the relationship between the strain mode and the displacement mode to obtain strain values and displacements. Borgert et al. [6] of NASA Langley Research Center combined the strain with finite element analysis to clarify the universal applicability of the modal method, which could be used for the real-time aircraft wing deformation reconstruction. Bernasconi and Ewins [7] used the strain measured by the strain

gauges to normalize the modal strain field. Wang et al. [8] calculated the strain mode and the displacement mode of the beam structure through theoretical derivation. Then, the modal superposition principle was used to estimate the dynamic displacement of the beam structure.

Tessler proposed the inverse finite element method based on the least square variational equation. The inverse method referred to the inversion between the known quantity and the unknown quantity. The structural strain values were known, and then, the structural displacements were deduced. Based on the Mindlin plate theory of elasticity and the principle of minimum potential energy, the inverse finite element was established. Gherlone et al. [9] proposed the inverse finite beam element suitable for the beam shear and torsional deformation. The simulation results showed that the deformation estimation obtained by using the inverse finite beam element was similar to the finite element software. Furthermore, the inverse finite beam element had successfully investigated the static and dynamic deformation reconstruction of the rigid frame structures. Tessler et al. considered the influence of multilayer composite surface on in-plane deformation of the plate and extended the small deflection plate deformation theory to the deformation description of composite structural plate [10], which was called refined zigzag theory (RZT). Kefal et al. [11] proposed an improved iFEM formulation for displacement and stress monitoring of laminated composite, sandwich plates, and shells. The advantage of the current formulation was that highly accurate through the thickness distributions of displacements, strain, and stresses were attainable using an element based on simple C^0-continuous displacement interpolation functions.

Many scholars have done a lot of research on the displacement-strain relationship. Ko et al. [12, 13] of NASA Dryden Flight Research Center proposed the KO displacement theory based on the piecewise linearization method and extended the theory to different load forms and different structures. The strain sensors were embedded on the surface of the beam. Then, the KO displacement equation was formulated with the strain data. The displacement equation was established with the measured (or finite element generated) strain data. Finally, the deflection and the cross-sectional twist angle of the beam were calculated. In 2009, the KO displacement theory was applied to the deformed shape analysis of the doubly tapered wings of the Ikhana unmanned aircraft [14].

Yi et al. [15] proposed a 3D surface reconstruction algorithm that transformed the strain into the discrete curvature of structure. Meng et al. [16] derived and fitted the deflection function of antenna array bending by strain on the surface of the antenna array unit panel, to achieve the deformation monitoring of the satellite antenna array unit. Currently, many strain sensors are needed to get more data to improve higher reconstruction accuracy. The strain measurement paths are also needed to be established based on the wing model before measurement. If the strain measurement paths and points are decided randomly, piecewise linearization during the following reconstruction process will accumulate great system error and the results are incredible.

With the development of artificial intelligence technology, intelligent algorithms are gradually applied to the area of wing deformation reconstruction. Shuo et al. [17] used a RBF neural network prediction model to realize high-precision numerical simulation. Siyuan et al. [18] proposed a fuzzy network method for real-time deformation measurement of airfoil antenna. Experiments were carried out on a flexible wing plate with 1200 mm length and 200 mm width. The maximum displacement in the training set of the fuzzy network method was 132.49 mm. The relative error of predicted displacement was 0.00019%. The maximum displacement in the test set was 108.98 mm. The relative error of predicted displacement was 1.535%. Fu et al. [19] combined fuzzy network and inverse finite element method to detect the deformation of the variable cross-section beam structure. Variable cross-section beam structure was a flexible structure with 1500 mm length and 200 mm width. The maximum displacement could reach about 150 mm. Dynamic load test on the variable cross-section wing model showed that the deformation reconstruction error obtained by the modified strain measurement was lower than 6.7%. Mao [20] proposed a linear neural network method for the deformation reconstruction of truss beam, which was not based on the specific object model. In this method, a linear mapping relationship between strain and displacement was assumed and the neural network was selected to identify and approximate such relationships. Chunhua et al. [21] developed a corrugated skin configuration to meet the requirements of the wing skin large deformation and constructed a radial basis function (RBF) neural network model with the current signal as input and the deformation as output. The average and maximum relative errors of the predicted displacement were 2.13% and less than 6%, respectively. Bao et al. [22] proposed a self-structuring fuzzy network (SSFN) method suitable for real-time measurement of the wing long-baseline antenna deformation. The experiment was carried out on the aluminum wing plate model with the static load. Xiao et al. [23] selected the BP neural network for the deformation calculation of the composite plate and used the data measured by laser displacement sensors and fiber grating sensors to train the BP neural network, which can be used to realize the composite plate deformation reconstruction. There are certain mapping relationships between strain values and displacements while the intelligent algorithm method is used for deformation reconstruction. The mapping relationships that do not depend on the research structure can be established. At present, all the studies are aimed at model structures with single-point concentrated loads. It is difficult to monitor and reconstruct the structural deformation precisely under multi-point or distributed complex load conditions.

For the existing problems of the structural deformation reconstruction, a wing deformation reconstruction algorithm, named PSO-RR (particle swarm optimization-ridge regression), was proposed. This algorithm established the mathematical model between strain points and displacement measurement points. The mathematical model could be independent of complex structures. It had high deformation reconstruction accuracy when the number of sensors was small. The structural deformation under different complex

load conditions could also be predicted precisely. For the study, an aluminum plate cantilever beam was selected as the research object, 34 different complex typical load cases were applied to the structure, and the strain values of specified points were obtained. Theoretical models of deformation point displacements and strain values were established by the ridge regression algorithm, and model ridge parameters were optimized through PSO algorithm. Subsequently, test results showed that the reconstruction deformation accuracy of the cantilever beam under complex working conditions was high. Finally, this method was applied to the specific complex aircraft wing structures, and ideal results were achieved.

2. The Deformation Reconstruction Principles of PSO-RR Algorithm

2.1. Ridge Regression Algorithm. Ridge regression [24] is a biased estimation regression method after the improvement of least squares regression, which abandons the unbiased property of least squares to obtain a more practical regression process [25]. Ridge regression attempts to address the bias-variance in the linear regression models. A nonlinear form of ridge regression can be obtained by reformulating ridge regression in dual variables using the well-known kernel method [26]. The ridge regression can be used to establish the theoretical model between the measured strain values of structural deformation and the displacement values of deformation reconstruction prediction points.

We suppose that there are M strain measuring points and N displacement measuring points on the surface or inside of the structure. The structure is subjected to K times of loads at different positions and under different load conditions to generate elastic recoverable deformation. Then, the strain matrix of all the measurement points and load cases is shown in equation (1), and the real measurement displacement matrix and predicted displacement matrix of the structures are shown in equations (2) and (3).

$$X^{\text{ridge}} = \begin{bmatrix} x_{11} & x_{12} & \cdots & x_{1M} \\ x_{21} & x_{22} & \cdots & x_{2M} \\ \vdots & \vdots & & \vdots \\ x_{K1} & x_{K2} & \cdots & x_{KM} \end{bmatrix}, \tag{1}$$

$$Y^{\text{ridge}} = \begin{bmatrix} y_{11} & y_{12} & \cdots & y_{1K} \\ y_{21} & y_{22} & \cdots & y_{2K} \\ \vdots & \vdots & & \vdots \\ y_{N1} & y_{N2} & \cdots & y_{NK} \end{bmatrix}, \tag{2}$$

$$\widehat{Y}^{\text{ridge}} = \begin{bmatrix} \widehat{y}_{11} & \widehat{y}_{12} & \cdots & \widehat{y}_{1K} \\ \widehat{y}_{21} & \widehat{y}_{22} & \cdots & \widehat{y}_{2K} \\ \vdots & \vdots & & \vdots \\ \widehat{y}_{N1} & \widehat{y}_{N2} & \cdots & \widehat{y}_{NK} \end{bmatrix}, \tag{3}$$

where $\widehat{Y}^{\text{ridge}} = X^{\text{ridge}}\omega$ and ω is the regression coefficient matrix. The size of ω is $M \times N$. The ridge regression loss function is defined as

$$L(\omega) = \left\| \widehat{Y}^{\text{ridge}} - Y^{\text{ridge}} \right\|_2^2 + \lambda \|\omega\|_2^2, \tag{4}$$

where λ is the ridge parameter. The gradient of the loss function can be expressed as

$$\begin{aligned} \frac{\partial L(\omega)}{\partial \omega} &= \frac{\partial}{\partial \omega}\left(\left\| X^{\text{ridge}}\omega - Y^{\text{ridge}} \right\|_2^2 + \lambda \omega^T \omega \right) \\ &= \frac{\partial}{\partial \omega}\left[\left(X^{\text{ridge}}\omega - Y^{\text{ridge}} \right)^T \left(X^{\text{ridge}}\omega - Y^{\text{ridge}} \right) + \lambda \omega^T \omega \right] \\ &= 2\left(X^{\text{ridge}} \right)^T X^{\text{ridge}}\omega - 2\left(X^{\text{ridge}} \right)^T Y^{\text{ridge}} + 2\lambda\omega, \end{aligned} \tag{5}$$

making $\partial L(\omega)/\partial \omega = 0$; the global optimal solution is obtained:

$$\omega^{\text{ridge}} = \left[\left(X^{\text{ridge}} \right)^T X^{\text{ridge}} + \lambda I \right]^{-1} \left(X^{\text{ridge}} \right)^T Y^{\text{ridge}}, \tag{6}$$

where ω^{ridge} is the ridge regression estimation. ω^{ridge} can be determined through the training data of the K times loads. When an unknown load is applied to the structure, the predicted displacement value of ridge regression can be obtained according to ω^{ridge}. In the ridge regression deformation reconstruction model, the choice of the ridge parameter λ directly affects the prediction result. Therefore, the relative error average of the predicted displacement is used as the performance index, and the PSO algorithm is used to obtain the optimal λ value.

2.2. PSO Algorithm. PSO algorithm is a group-based intelligent optimization search method [27], which is developed by Dr. Kennedy and Dr. Eberhart [28]. This algorithm mimics the social behavior patterns of the bird flock. This pattern is based on the intelligence of every individual and also influenced the collective behavior of the flock. The PSO algorithm model a problem into a space. Each particle has velocity and position. Particles evaluate their position and move towards to target which is the best position of the herd. This process is performed until the maximum iteration is reached [29, 30]. It is assumed that the potential solution of each ridge parameter in the ridge regression calculation is a particle in the search space, and all particles constitute a particle swarm. The particle swarm is randomly initialized in a given solution space. Each particle has an initial position and velocity, and the λ is searched in the solution space by iterative optimization [31].

It is supposed that in a D-dimensional target search space, a community is formed by P particles, where the ith x_i particle is represented as a D-dimensional vector:

$$x_i = (x_{i1}, x_{i2}, \cdots, x_{iD}), i = 1, 2, \cdots, P. \quad (7)$$

The flying speed of the particle is also a D-dimensional vector, denoted as

$$v_i = (v_{i1}, v_{i2}, \cdots, v_{iD}), i = 1, 2, \cdots, P. \quad (8)$$

The optimal position of the particle searched is called the individual optimal value, expressed as follows:

$$p_{\text{best}} = (p_{i1}, p_{i2}, \cdots, p_{iD}), i = 1, 2, \cdots, P. \quad (9)$$

The optimal position of the entire particle swarm searched is called the global optimal value, which is recorded as

$$g_{\text{best}} = (g_1, g_2, \cdots, g_D). \quad (10)$$

When these two optimal values are found, the velocity and position of the particles are updated according to

$$v_{ij}(t+1) = v_{ij}(t) + c_1 r_1(t)\left[p_{ij}(t) - x_{ij}(t)\right] + c_2 r_2(t)\left[g_j(t) - x_{ij}(t)\right], \quad (11)$$

$$x_{ij}(t+1) = x_{ij}(t) + v_{ij}(t+1),\ i = 1, 2, \cdots, P, j = 1, 2, \cdots, D, \quad (12)$$

where c_1 and c_2 are learning factors, r_1 and r_2 are random numbers between 0 and 1, v_{ij} is the speed of the particle, $v_{ij} \in [-v_{\max}, v_{\max}]$, and $v_{\max}$ is a constant, used to limit the speed of the particle.

The position of each particle is substituted into the ridge regression model. The predicted displacement value $\widehat{Y}^{\text{ridge}}$ is calculated. The average relative error between $\widehat{Y}^{\text{ridge}}$ and the real displacement value Y^{ridge} is used as the fitness of the particle, which is evaluated whether the particle reaches the optimal position.

The flow chart of the optimization process is shown in Figure 1.

The particle position corresponding to the global optimal value of the PSO is the optimized ridge parameter. It is used to predict the deformation under the other load cases, thereby the optimal deformation reconstruction model is established.

3. Experimental System of Airfoil Cantilever Beam

To check the effectiveness of the PSO-RR method on actual wing structures, the airfoil cantilever beam was taken as the research object. The length of the beam was 500 mm (excluding the fixed part), the fixed end width was 100 mm, the free end width was 50 mm, and the thickness was 3 mm. The material was aviation aluminum alloy, elastic modulus 71 GPa, Poisson's ratio 0.3, and density 2.81 g/cm^3. End-fixed support was shown in Figure 2.

The cantilever beam was arranged with fifteen concentrated loading points at equal intervals along the sides and center lines. Five strain measurement points were arranged at equal intervals along the upper side of the cantilever beam from the fixed end to the free end, and another five strain points were arranged at another symmetric side, shown in Figure 2. According to the analysis results of the model finite element under different load cases and the experience of previous research, the number and arrangement of strain measurement points were determined.

Strain-type sensors were used in the experiment. The loading point positions and strain-type sensors on the test model were shown in Figure 3. The right side in the figure was the fixed end of the cantilever beam.

Four displacement measurement points were selected on the free end of the cantilever beam. The specific positions were shown in Figure 4, and the deformation displacement in the vertical direction was measured by the laser displacement sensor when the load was applied. A laser displacement sensor was placed on the table, as shown in Figure 5. The displacement measurement point was irradiated with the laser point from the laser displacement sensor. The initial position was recorded and set to zero by the laser displacement sensor when the structure was not loaded. The vertical direction deformation was recorded directly when the structure was loaded with small deformation. When the structure was loaded with large deformation, the laser point would offset from the original displacement measurement point. It was necessary to move the laser displacement sensor horizontally to ensure the displacement measurement point was irradiated with the laser point again. Then, the deformation was recorded in the vertical direction.

Each load point had a through-hole with a diameter of 2 mm. One end of the light nylon wire was passed through the hole and fixed with a thread locking device; another end was hung with weights to exert static load on the beam. The loading mode of weights was shown in Figure 6.

A multichannel strain measurement system and a laser displacement sensor were selected to test the strain values and displacement values. The experimental system was shown in Figure 5. The strain measurement system consisted of double-bar T-type strain gauge BE120-2BB (23), multichannel strain gauge (TST3828E), and its supporting software. Each T-type strain gauge contains two sensitive grids which were perpendicular to each other. Therefore, the longitudinal and transverse strain of the beam could be measured at the same time. Before each test, the strain gauge was set to zero to eliminate the influence of additional weights, such as beam deadweight, the wire, wire locks, and nylon wire.

4. Experimental Load Cases of the Beam

To verify the influence of different load cases on the beam deformation, 34 different types of static concentrated load

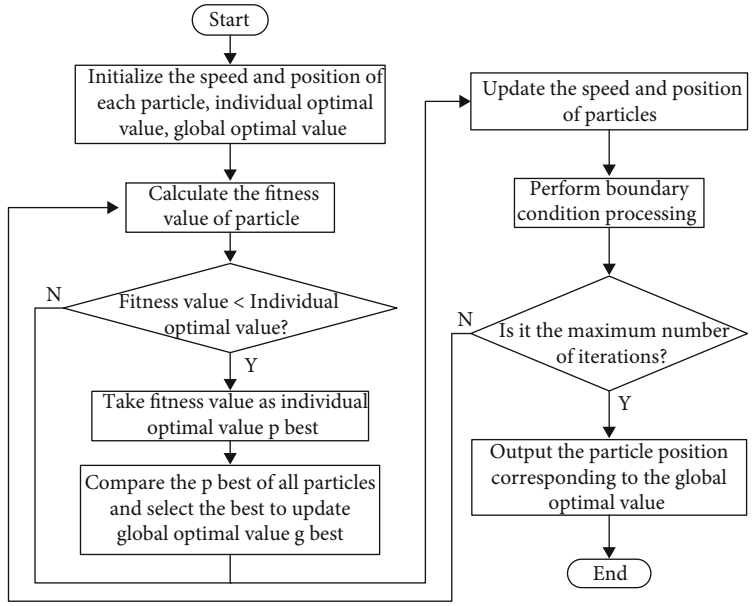

Figure 1: PSO algorithm flow chart.

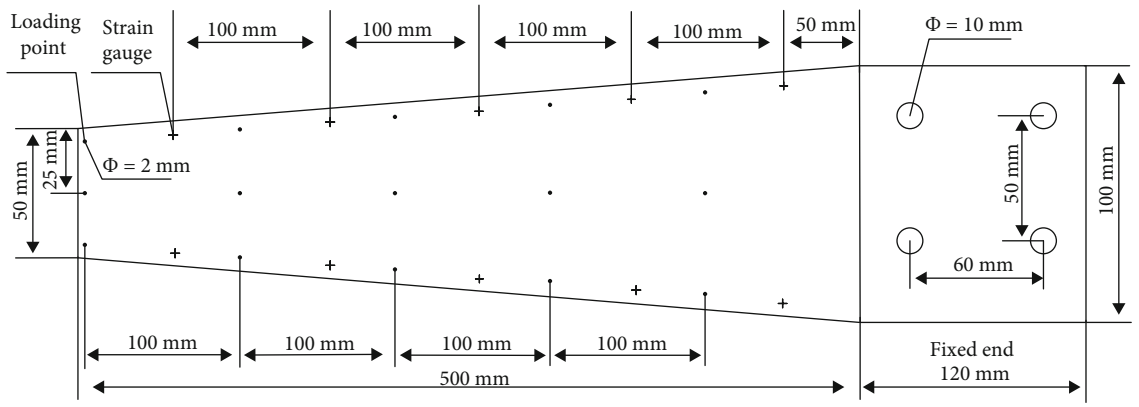

Figure 2: Airfoil cantilever structure diagram.

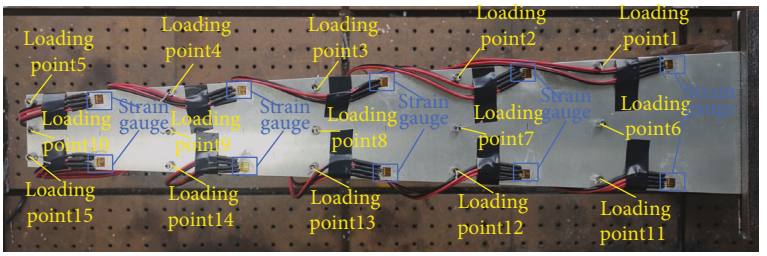

Figure 3: Cantilever beam model with sensors.

cases were adopted, as shown in Table 1. The load was positive in the direction of gravity and negative in the opposite direction. The flow chart of the whole experiment was shown in Figure 7. Loading tests with different kinds of load cases was shown in Figure 8.

5. Static Load Test Results of Cantilever Beam

Strain values were obtained after all the tests, but the accuracy of the test results lacked quantitative evaluation [32]. Therefore, it was necessary to analyze the measurement

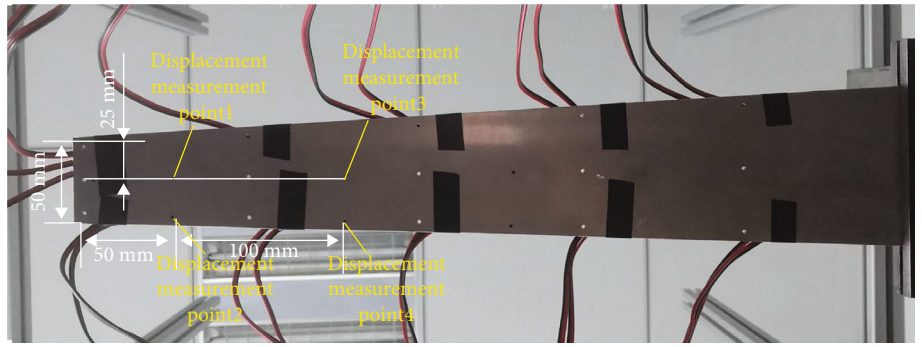

Figure 4: Layout of displacement measuring points.

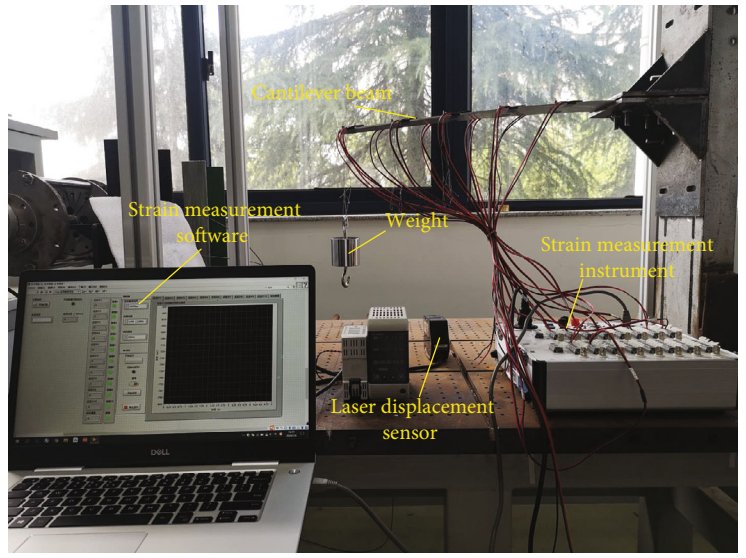

Figure 5: The whole experimental system.

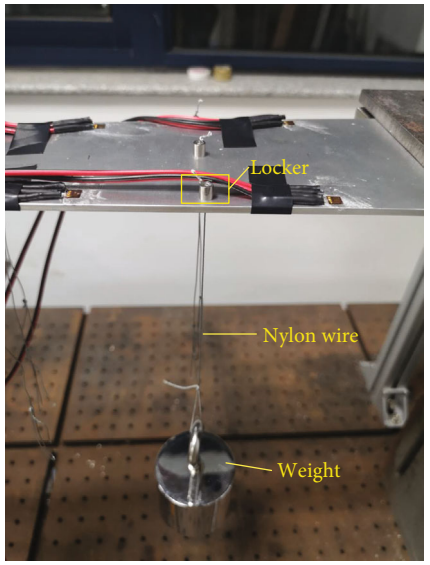

Figure 6: Static loading form.

errors during the experiment process and determine the uncertainty to evaluate the reliability of the test. During the test process, many factors, such as stability and precision accuracy of test instruments, the vibration of surrounding environment, temperature changes, model consistency after each load replacement, and so on, could affect the test accuracy. In every experiment, each strain measurement point was continuously collected 50 strain values. The accuracy and uncertainty of the test results were analyzed as follows.

Considering the longitudinal strain data of one strain point with load case 1, shown in Table 1, as an example. Test results of longitudinal strain were $x_k (k = 1, 2, \cdots, 50)$. The x_k average value was

$$\bar{x} = \frac{1}{50}\sum_{k=1}^{50} x_k = -4.01\mu\varepsilon. \tag{13}$$

The experimental standard deviation of the strain point with load case 1 was

Table 1: Static load cases.

Load case	Load form	Loading point	Loading
1 ~ 15	Single point concentrated load	1 ~ 15 each load point was applied with concentrated load	10 N
16	Edge load	1, 6, 11	10 N, 10 N, 10 N
17		2, 7, 12	10 N, 10 N, 10 N
18		3, 8, 13	10 N, 10 N, 10 N
19		4, 9, 14	10 N, 10 N, 10 N
20		5, 10, 15	10 N, 10 N, 10 N
21	Gradient edge load	1, 2, 3, 4, 5	10 N, 10 N, 10 N, 10 N, 10 N
22		6, 7, 8, 9, 10	10 N, 10 N, 10 N, 10 N, 10 N
23		11, 12, 13, 14, 15	10 N, 10 N, 10 N, 10 N, 10 N
24		1, 2, 3, 4, 5	25 N, 20 N, 15 N, 10 N, 5 N
25		6,7,8,9, 10	25 N, 20 N, 15 N, 10 N, 5 N
26		11, 12, 13, 14, 15	25 N, 20 N, 15 N, 10 N, 5 N
27	Torsional load	2, 12	-50 N, 5 N
28		3, 13	-50 N, 5 N
29		3, 13	-20 N, 5 N
30		3, 13	-30 N, 10 N
31		4, 14	-30 N, 5 N
32		4, 14	-30 N, 10 N
33		5, 15	-20 N, 5 N
34		5, 15	-20 N, 10 N

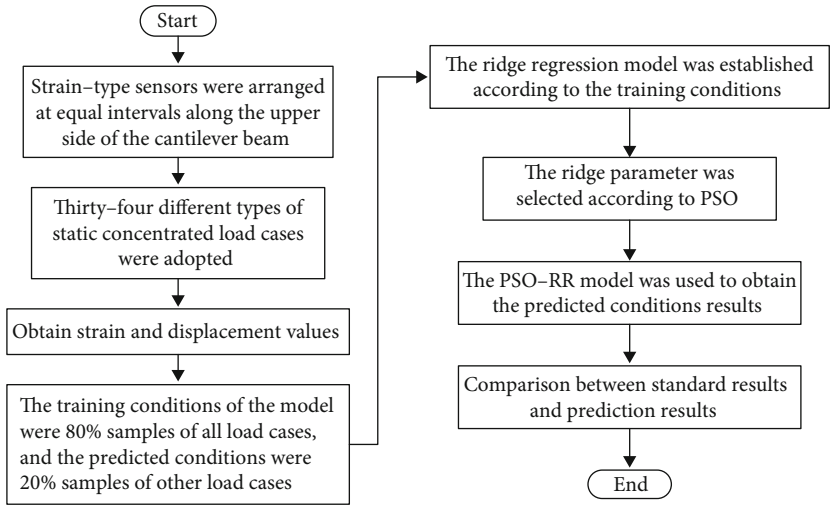

Figure 7: Flow chart of methodology.

$$s(x_k) = \sqrt{\frac{\sum_{k=1}^{50}(x_k - \bar{x})^2}{50-1}} = 0.16\mu\varepsilon. \quad (14)$$

In addition, this strain point also had the test data from load case 2 to load case 34. In each load case, 50 groups of test data were continuously collected, and a total of 34 groups x_k were obtained. The combined standard deviations of this strain point with 34 load cases were calculated, shown in Figure 9. The average of this strain point under 34 load cases was shown in Table 2.

The combined standard deviation of this strain point was

$$s_p(x_k) = \sqrt{\frac{\sum_{j=1}^{34}\left[s_j(x_k)\right]^2}{34}} = 0.23\mu\varepsilon. \quad (15)$$

The uncertainty of this strain point was

$$u(\overline{x_k}) = \frac{s_p(x_k)}{\sqrt{50}} = 0.03\mu\varepsilon. \quad (16)$$

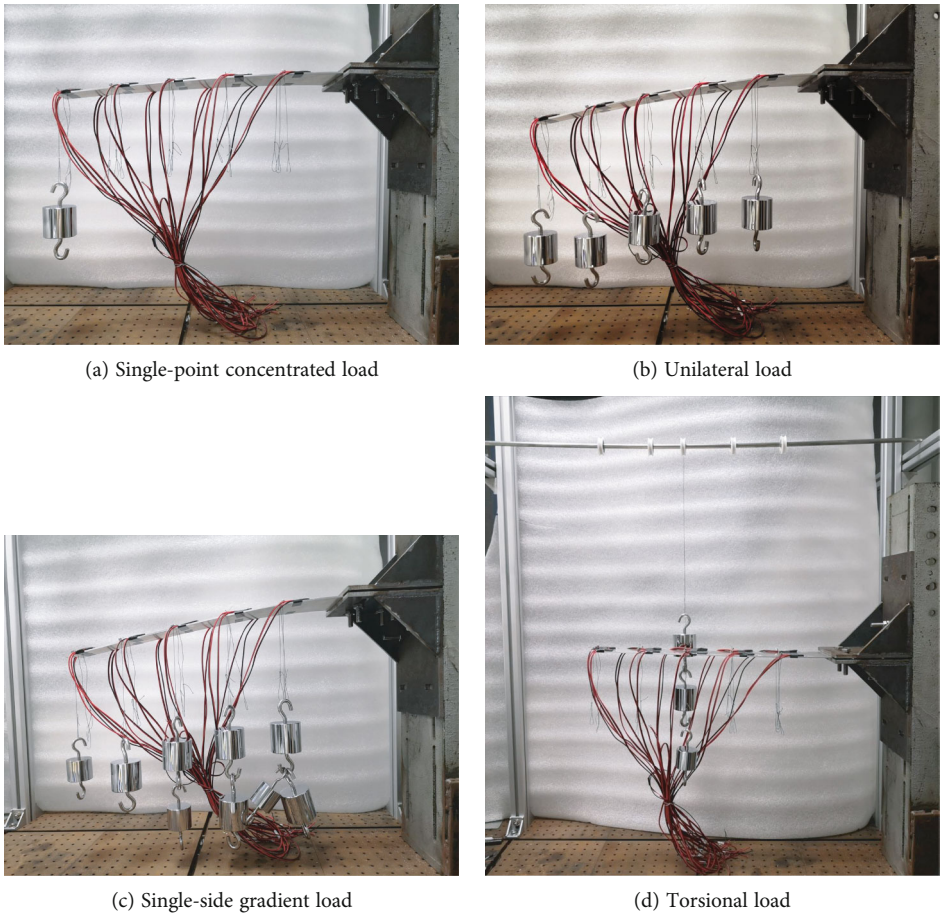

(a) Single-point concentrated load

(b) Unilateral load

(c) Single-side gradient load

(d) Torsional load

Figure 8: Experimental diagrams with different load cases.

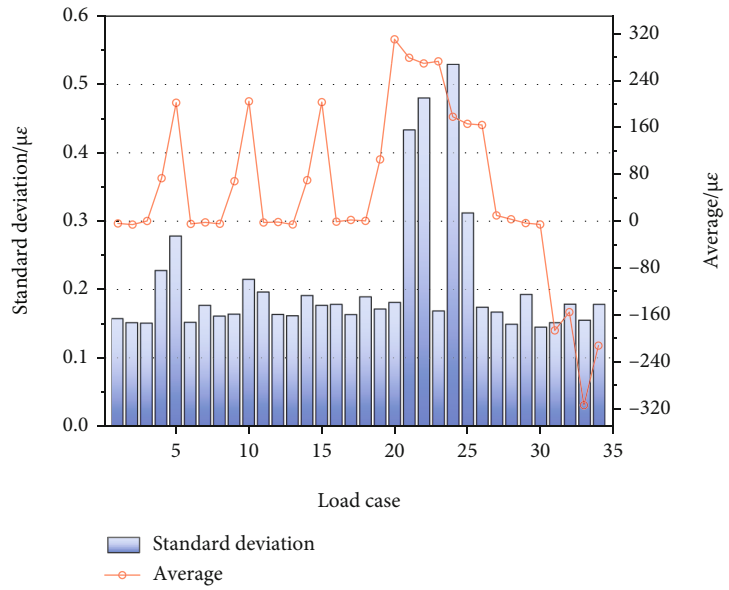

Figure 9: Standard deviation and average of all load cases of one strain point.

Table 2: Strain average of one strain point under 34 load cases.

Load case	1	2	3	4	5	6	7	8	9
Strain average ($\mu\varepsilon$)	-4.01	-5.89	0.24	73.19	202.15	-4.69	-2.08	-4.51	68.18
Load case	10	11	12	13	14	15	16	17	18
Strain average ($\mu\varepsilon$)	204.47	-2.45	-1.57	-5.71	69.85	203.07	-1.01	1.95	0.30
Load case	19	20	21	22	23	24	25	26	27
Strain average ($\mu\varepsilon$)	105.25	310.38	278.88	269.24	272.83	178.18	166.10	164.03	9.72
Load case	28	29	30	31	32	33	34		
Strain average ($\mu\varepsilon$)	3.25	-3.36	-5.77	-186.71	-155.38	-314.31	-212.65		

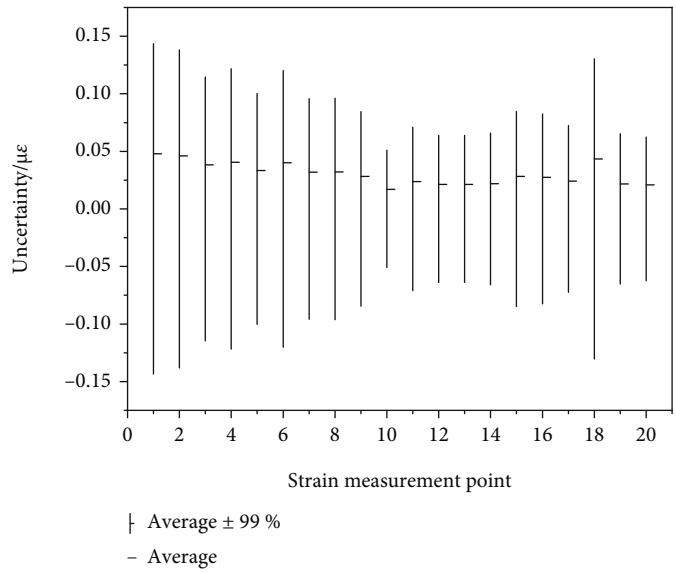

Figure 10: Expanded uncertainty of all the strain points.

Uncertainties of other strain points can be obtained with the same analysis method. If the confidence interval was 99.74%, the expanded uncertainty of each strain point was $U = k_p u(\overline{x_k})$, $k_p = 3$, shown in Figure 10.

The laser displacement sensor had very high accuracy, less than one micron. Therefore, the test results of four displacement points under all load cases were set to the exact values, shown in Table 3.

5.1. Experiments of Ridge Regression Model Prediction. To consider the uncertainty of the strain measurement system into the displacement prediction result, the Monte Carlo method (MCM) was used here [33, 34]. The basic idea was to establish the theoretical model between input and output data. The input data with uncertainty were obeyed the probability density distribution. Then, the output data of the theoretical model had statistical uncertainty.

Steps of Monte Carlo uncertainty evaluation method for deformation reconstruction test based on ridge regression model are as follows:

Step 1: Monte Carlo data and model

(a) Define the output data. In this deformation reconstruction test, it was the displacement value matrix, Y, of the four displacement measurement points

(b) Define the input data. All the strain test data matrix under all load cases, $x_{\text{strain1}}, x_{\text{strain2}}, \cdots x_{\text{strain20}}$, were the input data. The uncertainty of all this data was shown in Figure 9

(c) Build the models between input data, x_{strain1}, $x_{\text{strain2}}, \cdots x_{\text{strain20}}$, and output data Y. Ridge regression method was selected to establish this theoretical model between input and output data

(d) Set the probability density function for the input data to conform to a uniform distribution. Based on Figure 9

(e) Choose the size of the Monte Carlo trials number, M. In the experiment, M was selected as $M = 106$. It would provide a 95% confidence interval for the output data Y

Step2: Monte Carlo spread

(a) Extract 10^6 sample input data from the probability density distribution function of the input data, $x_{strain1}, x_{strain2}, \cdots x_{strain20}$

(b) Calculate the output data of all sample input data based on the model

Step3: Monte Carlo output and results

(a) Sort the output data in strictly increasing order. The output distribution function was obtained by the sorting model

(b) Obtain the final predicted deformation displacements with uncertainty. The output data of this model were the predicted values

The test results of the four displacement points under all load cases were used as the exact values. Test results of all the strain points under all load cases were the input data of the ridge regression model. The ridge parameter, λ, was initially set to 0.1. The training conditions of the model were 80% samples of all load cases, and the predicted conditions were 20% samples of other load cases. The purpose of randomly dividing all the data into the training set and the test set was to verify the algorithm accuracy in unknown load cases. Usually, the structure would be tested on the ground and in the wind tunnel. The ground experiment provided a limited number of load cases. Man unknown loads were produced in the wind tunnel experiments. The algorithm also needed to calculate the structural deformation according to the strain points under unknown load. Therefore, 20% samples of all load cases were randomly selected as the unknown load test set.

Training samples and prediction samples were randomly selected from all 34 load cases three times. Predicted displacements and corresponding exact values were shown in Figure 11. In a total of 34 load cases, the first random prediction load cases numbers were 3, 13, 15, 22, 25, 32, ad 34. The second random prediction load cases numbers were 10, 12, 16, 17, 20, 28, and 31. The third random prediction load cases numbers were 1, 6, 15, 16, 22, 27, and 31.

In Figure 11, EV meant exact value and PV meant predicted value. Figures 11(a)–11(c)were exact and predicted displacements of displacement point in three-times prediction. The legends in (b) and (c) were the same as (a). Figures 11(d)–11(f) were the corresponding absolute errors. The legends in (e) and (f) were the same as (d). From Figure 11, we found that the maximum absolute error was 4.79 mm while the deformation displacement was 26.02 mm, and the average absolute error of the three random predictions was 1.42 mm, 2.06 mm, and 1.72 mm, respectively. All the average absolute error was 1.73 mm.

5.2. Experiments of PSO-RR. The parameter λ, in the ridge regression model, had a direct effect on the prediction results. PSO algorithm was used to obtain the optimized parameter λ. The dimension of PSO search space was $D = 1$, the number of particles $N = 100$, $c_1 = c_2 = 1.5, v_{max} = 1$ based on early experiences. The results were shown in Figure 12. Three prediction condition numbers were the same as Figure 11.

Figures 12(a)–12(c) were the RR parameter, λ, optimization iteration curve, and the final parameters of the three predictions were 9.90×10^{-2}, 5.93×10^{-2}, and 8.95×10^{-2}, respectively. The legends in (e) and (f) were the same as (d), and in (h) and (i) were the same as (g). From Figures 12(g)–12(i), we found that the maximum absolute error between the prediction and exact result was less than 4.47 mm. The average absolute errors of the three random predictions were 0.85 mm, 1.47 mm, and 1.69 mm, respectively. The average absolute error of all the results was

Table 3: Test results of four displacement points (unit: mm).

Load cases	Displacement measurement point (mm)			
	1	2	3	4
1	5.54	5.66	4.24	4.37
2	11.68	11.56	8.76	8.76
3	11.72	11.98	8.46	8.19
4	18.98	19.24	12.83	12.69
5	26.19	25.91	16.90	17.06
6	5.64	5.78	4.35	4.11
7	11.77	11.94	8.68	8.59
8	11.80	11.65	8.39	8.51
9	18.93	18.90	12.72	12.72
10	26.20	26.02	16.81	16.74
11	5.39	5.56	4.18	4.32
12	11.82	11.84	8.73	8.99
13	11.77	11.76	8.37	8.09
14	18.99	18.74	12.76	12.78
15	26.13	25.98	16.84	16.69
16	5.51	5.35	4.28	4.24
17	17.44	17.60	12.92	12.71
18	17.66	17.44	12.55	12.37
19	28.20	28.43	18.96	18.73
20	38.69	38.58	25.33	25.39
21	62.32	62.05	42.22	42.50
22	62.45	62.67	42.26	42.05
23	62.40	62.64	42.29	42.11
24	63.41	63.23	44.02	43.94
25	63.53	63.81	44.15	44.14
26	63.20	63.12	43.93	44.02
27	-27.08	-26.68	-20.07	-20.14
28	-52.38	-51.88	-37.24	-36.89
29	-17.76	-17.84	-12.93	-12.85
30	-24.17	-23.62	-17.05	-17.42
31	-47.50	-48.35	-32.24	-31.98
32	-37.89	-38.26	-25.69	-25.33
33	-39.71	-39.53	-25.53	-25.55
34	-26.80	-26.51	-17.14	-17.24

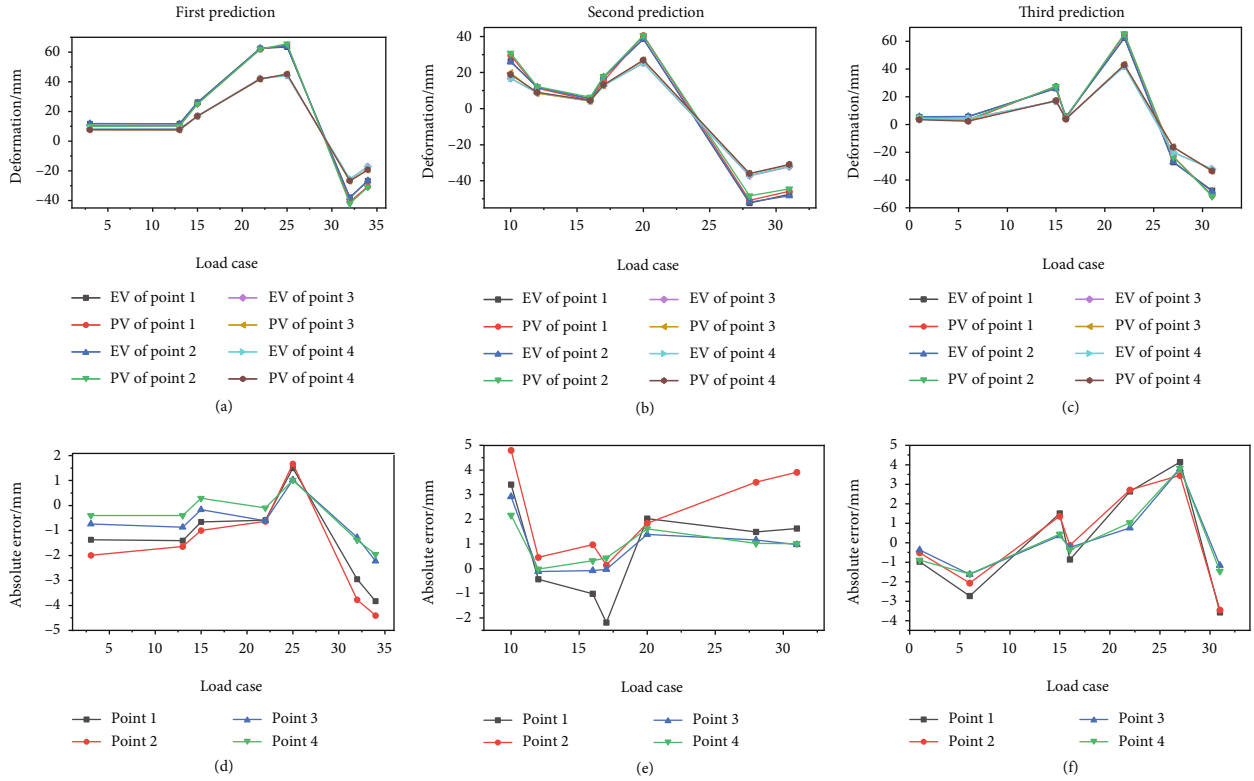

Figure 11: Predicted and exact values of displacement of RR method.

1.34 mm. It was lower than the prediction result in section 5.1. All errors were less than 2 mm, and three times training conditions can include all load forms such as single-point concentrated load, unilateral load, single-side gradient load, and torsional load. After parameter optimization, the average prediction accuracy has been significantly improved. The test results showed that the PSO-RR prediction method had higher accuracy.

5.3. Comparative Analysis and Research of KO Displacement Theory Method and PSO-RR Method. To verify the prediction accuracy of the PSO-RR method, the typical deformation reconstruction method, KO displacement theory [35], was selected as another method. It needed to establish a strain measurement path from the fixed end of the cantilever beam to the free end. Then, the deformation curve in sections based on the strain measurement points in the path could be reconstructed. Finally, the displacements of the free end could be obtained.

Since displacement points 2 and 4, shown in Figure 4, were at the end of the strain measurement path, these two points were selected as comparative analysis. Four different load cases from single-point load, unilateral load, unilateral gradual load, and torsional load were selected randomly. Experiment and analysis results of the two different methods were shown in Table 4.

From Table 4, the maximum absolute errors of PSO-RR and KO methods were 2.12 mm and 3.96 mm. The average absolute errors of PSO-RR and KO for displacement point 2 were 1.0 mm and 1.89 mm, respectively, and 0.71 mm and 3.26 mm for displacement point 4, respectively. Experimental results showed that the PSO-RR method had hgher prediction accuracy than the KO theoretical method.

6. Application of PSO-RR Method on Real Wing Structures

The PSO-RR method was applied to the wing skeleton structure of an aircraft. The static tests of the wing under different load cases were carried out. Eight displacement measurement points were arranged on the wing surface, shown in Figure 13. 177 strain measurement points were arranged at the front beam, rear beam, and panel. There were too many measurement points to mark out in Figure 13. The schematic diagram of wing size was shown in Figure 13, and the 3D digital model of the wing structure was shown in Figure 14.

In static load experiments, a hydraulic loading system was used. Hydraulic actuators were installed at the front and rear edges of each intercostal space for applying force, with a total of 14 loading points. The upward bending test was carried out with 5% of the test load as the first level. Subsequently, the load was increased by 5% each time and improved to 180% of the test load gradually after a 36 times increase. Then, the load was reduced by 5% each time and gradually unloaded to 0%.

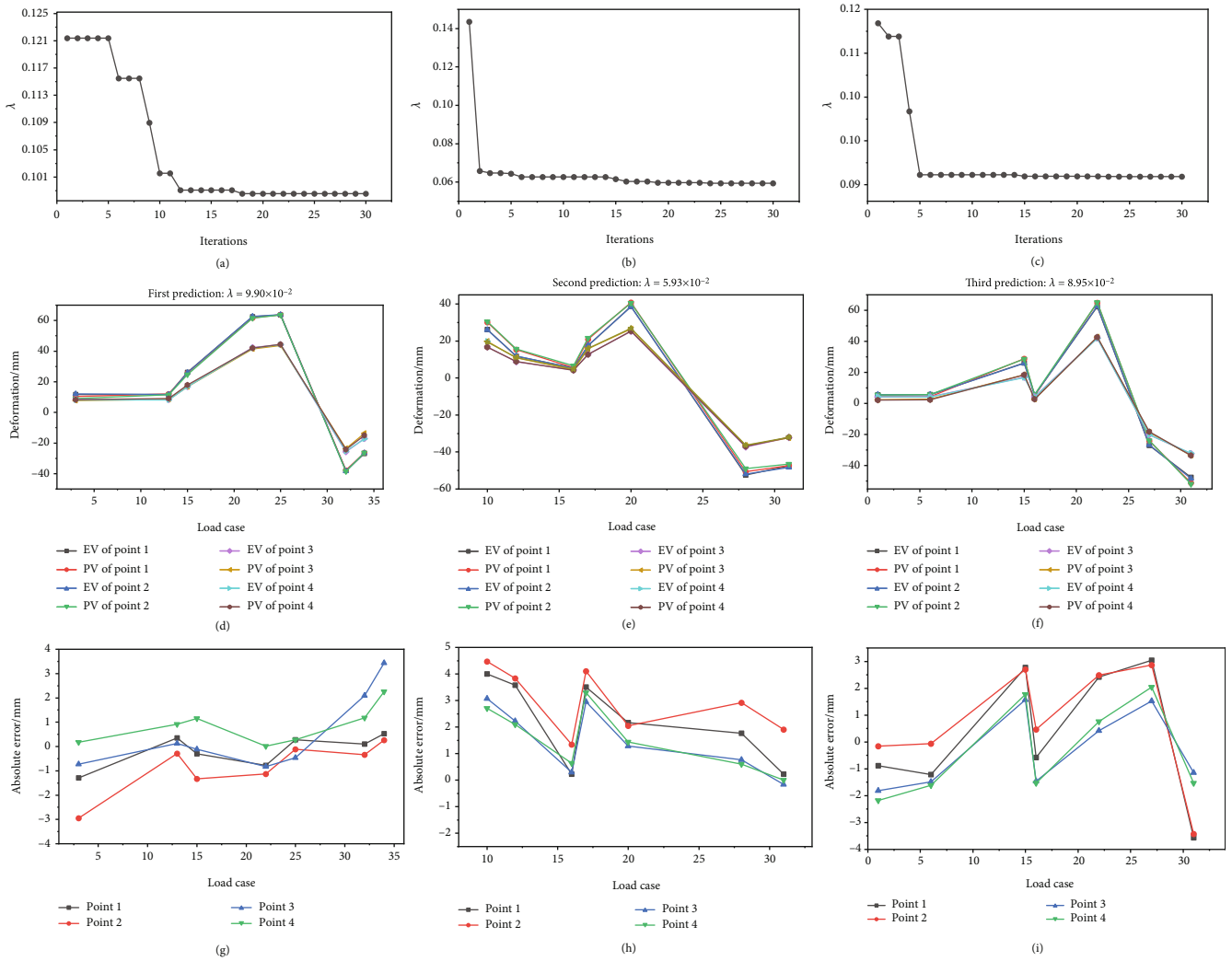

Figure 12: Predicted and exact values of displacement of the PSO-RR method.

Table 4: Analysis of PSO-RR and KO theoretical prediction results.

Load case	Displacement point 2					Displacement point 4				
	Deformation/mm			Absolute error/mm		Deformation/mm			Absolute error/mm	
	Exact value	PSO-RR	KO	PSO-RR	KO	Exact value	PSO-RR	KO	PSO-RR	KO
3	11.98	11.72	11.79	-0.26	-0.19	8.19	8.35	6.68	0.16	-1.51
17	17.60	17.07	16.90	-0.53	-0.70	12.71	13.22	10.32	0.51	-2.39
24	63.23	61.11	65.94	-2.12	2.71	43.94	42.02	36.54	-1.92	-7.40
34	-26.51	-27.61	-30.47	-1.10	-3.96	-17.24	-17.50	-15.47	-0.26	1.77

Therefore, a total of 71 load cases were considered. The strain values and displacements of all the test points were recorded under all 71 load case conditions. The test was shown in Figure 15.

Since the strain measurement points were located in the key position of the wing structure, the strain measurement path cannot be established. Therefore, the typical deformation reconstruction method, the KO theory method, was not applicable. Same as above, 80% of test results of all load cases, 56 load cases, were selected randomly for PSO-RR model training. Other 15 load cases were selected as the displacement prediction. The prediction results were shown in Figure 16.

The exact and predicted values of displacement from displacement point 1 to point 8 were shown in Figures 16(a) and 16(b). Figures 16(c) and 16(d) were the corresponding

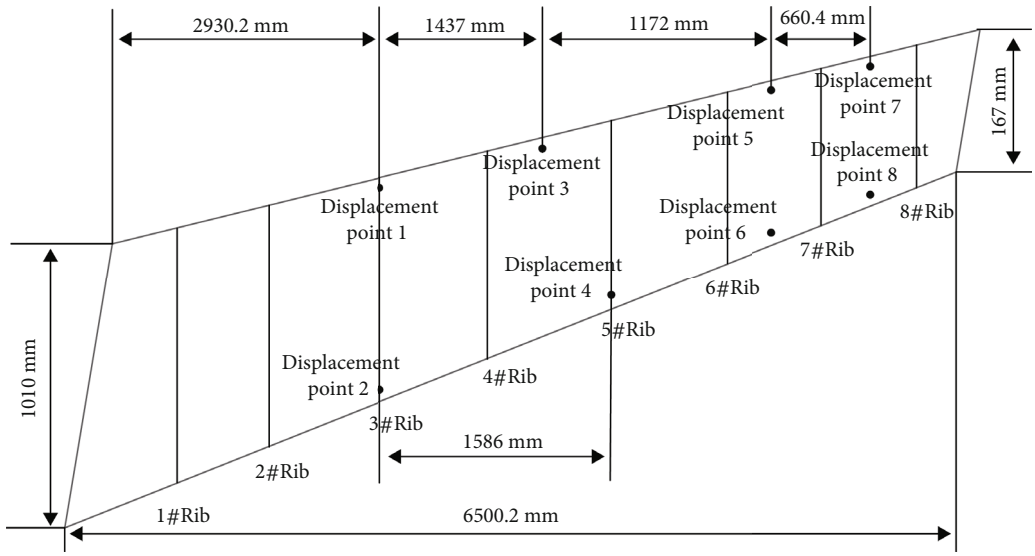

Figure 13: Schematic diagram of wing size.

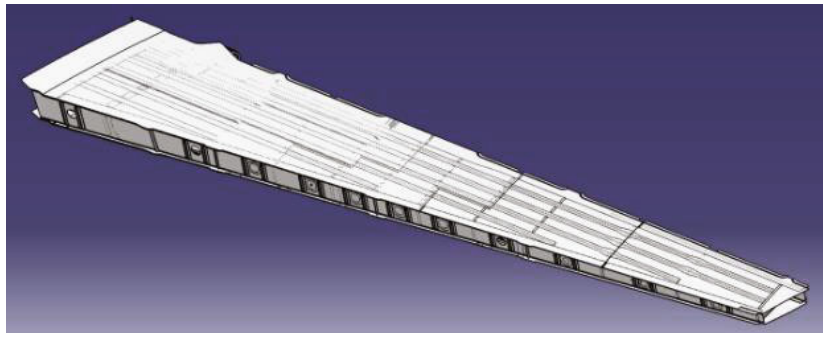

Figure 14: Three-dimensional digital model structure diagram of wing.

Figure 15: Static load experiments of wing structures.

absolute errors. The parameter was 5.93×10^{-2}. The maximum absolute error of all the displacement points was less than 1.2 mm, and the average absolute error of each displacement point was 0.16 mm, 0.26 mm, 0.34 mm, 0.36 mm, 0.69 mm, 0.18 mm, 0.68 mm, and 0.26 mm, respectively. Test results showed that the PSO-RR method could be used as the

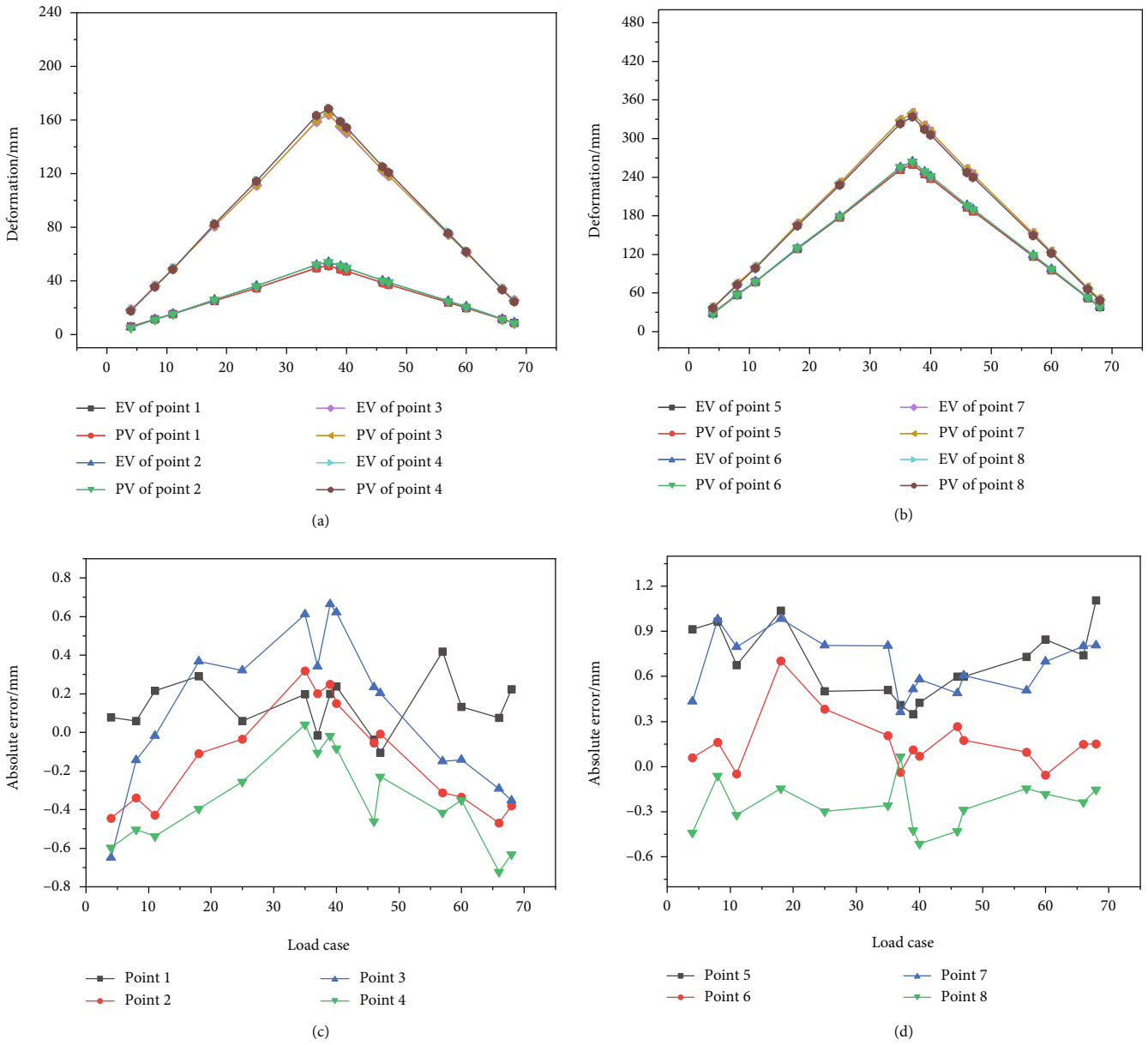

Figure 16: Comparison chart of displacement point prediction results.

deformation reconstruction of complex wing structures with complex load cases and had high accuracy.

7. Conclusions

Considering the need for real-time monitoring and deformation reconstruction of aircraft structures, the PSO-RR structure deformation reconstruction method was proposed. PSO-RR was different from other contact deformation measurement methods. It did not directly depend on the structural characteristics. Firstly, the theoretical model between the strain and deformation could be established through training data of different load cases. The theoretical model was used to predict structural deformation under unknown load cases. Secondly, PSO-RR was applied to complex real wing structures. The traditional contact measurement method had better experimental results on a simple structure with fewer strain sensors. But the real wing structure was more complex and there were many strain measurement points, the PSO-RR method could restore the structural deformation better. Thirdly, the PSO-RR could ignore the stress of the structure under complex load forms such as multipoint loading. It depended on the value of strain measuring points. The feasibility and reliability of PSO-RR were verified through experimental analysis of the airfoil cantilever beam. Three times of random prediction experiments were carried out on the airfoil cantilever beam. The average absolute error of the RR prediction result was 1.73 mm, and the average absolute error of the PSO-RR prediction result was 1.34 mm. The results proved that the PSO-RR had higher prediction accuracy. Compared with the KO deformation reconstruction method which was a typical

deformation reconstruction algorithm, PSO-RR had higher accuracy, smaller error, and more accurate deformation prediction. Finally, the PSO-RR algorithm was applied to the static loading experiment of a complex real aircraft. The maximum absolute error of all the eight displacement points was less than 1.2 mm. Test results showed that the method could predict the wing deformation displacement under different complex loads with high precision.

Data Availability

Some data included in this study are available upon request by contact with the corresponding author.

Conflicts of Interest

The authors declare that they have no conflicts of interest.

References

[1] S. Xiasheng and X. Yinchun, "Opportunities and challenges of aircraft structural health monitoring," *Acta Aeronautica et Astronautica Sinica*, vol. 35, no. 12, pp. 3199–3212, 2014.

[2] W. Bin, L. Jin, L. Jie, and R. Maodong, "3D full-field wing deformation measurement method for large high-wing airplanes," *Acta Aeronautica et Astronautica Sinica*, vol. 38, no. 7, pp. 172–181, 2017.

[3] J. Bartley-Cho, D. Wang, and J. Kudva, "Shape estimation of deforming structures," in *19th AIAA Applied Aerodynamics Conference*, p. 1566, Anaheim,CA,U.S.A, 2001.

[4] L. Lu, H. Song, Y. Wang, and C. Huang, "Deformation behavior of non-rigid airships in wind tunnel tests," *Chinese Journal of Aeronautics*, vol. 32, no. 3, pp. 611–618, 2019.

[5] G. C. Foss and E. D. Haugse, "Using modal test results to develop strain to displacement transformations," in *In Proceedings of the 13th international modal analysis conference*, p. 112, Nashville, TN, 1995.

[6] P. Bogert, E. Haugse, and R. Gehrki, "Structural shape identification from experimental strains using a modal transformation technique: AIAA/ASME/ASCE/AHS/ASC structures," in *Structural Dynamics, & Materials Conference*, p. 1626, Norfolk, Virginia, 2003.

[7] O. Bernasconi and D. J. Ewins, "Application of strain modal testing to real structures," *6th International Modal Analysis Conference*, 1998, pp. 1453–1464, Kissimmee, Florida, 1988.

[8] Z. C. Wang, D. Geng, W. X. Ren, and H.-T. Liu, "Strain modes based dynamic displacement estimation of beam structures with strain sensors," *Smart Materials and Structures*, vol. 23, no. 12, p. 125045, 2014.

[9] M. Gherlone, P. Cerracchio, M. Mattone, M. Di Sciuva, and A. Tessler, "Shape sensing of 3D frame structures using an inverse finite element method," *International Journal of Solids and Structures*, vol. 49, no. 22, pp. 3100–3112, 2012.

[10] A. Tessler, M. Di Sciuva, and M. Gherlone, "A refined zigzag beam theory for composite and sandwich beams," *Compos Mater*, vol. 43, no. 9, pp. 1051–1081, 2009.

[11] A. Kefal, I. E. Tabrizi, M. Yildiz, and A. Tessler, "A smoothed iFEM approach for efficient shape-sensing applications: numerical and experimental validation on composite structures," *Mechanical Systems and Signal Processing*, vol. 152, article 107486, 2021.

[12] C. V. Jutte, W. L. Ko, C. A. Stephens, J. A. Bakalyar, and W. L. Richards, *Deformed Shape Calculation of a Full-Scale Wing Using Fiber Optic Strain Data from a Ground Loads Test [M]*, National Aeronautics and Space Administration, Dryden Flight Research Center, 2011.

[13] W. L. Ko and V. T. Fleischer, "Extension of Ko straight-beam displacement theory to deformed shape predictions of slender curved structures," NASA Technical Report, 2011, https://ntrs.nasa.gov/citations/20110011037.

[14] W. L. Ko, W. L. Richards, and V. T. Fleischer, "Applications of Ko displacement theory to the deformed shape predictions of the doubly-tapered Ikhana wing," NASA Technical Report, 2009, https://ntrs.nasa.gov/citations/20090040594.

[15] J. Yi, X. Zhu, H. Zhang, L. Shen, and X. Qiao, "Spatial shape reconstruction using orthogonal fiber Bragg grating sensor array," *Mechatronics*, vol. 22, no. 6, pp. 679–687, 2012.

[16] G. Meng, H. Hanhui, and X. Dingbang, "A displacement detection method for satellite phased-array antenna based on strain measurement," *Spacecraft Environment Engineering*, vol. 29, no. 6, pp. 663–666, 2012.

[17] T. Shuo, S. Jianqin, and G. Pengtao, "Numerical simulation and deformation prediction of stress peen forming for integrally-stiffened panels," *Acta Aeronautica et Astronautica Sinica*, vol. 40, no. 10, pp. 279–291, 2019.

[18] F. Siyuan, B. Hong, and Z. Xudong, "An airfoil antenna deformation measurement method based on fuzzy network," *Modern Radar*, vol. 37, no. 11, pp. 59–63, 2015.

[19] Z. Fu, Y. Zhao, H. Bao, and F. Zhao, "Dynamic deformation reconstruction of variable section WING with fiber Bragg grating sensors," *Sensors (Basel)*, vol. 19, no. 15, p. 3350, 2019.

[20] Z. Mao and M. Todd, "Comparison of shape reconstruction strategies in a complex flexible structure," *In Sensors and Smart Structures Technologies for Civil, Mechanical, and Aerospace Systems 2008*, vol. 6932, pp. 127–138, 2008.

[21] Z. Chunhua, W. Bangfeng, L. Zhao, C. Heng, and M. Changwei, "Drive control and neural network modeling of corrugated skin with initiative deformation," *Ordnance Material Science and Engineering*, vol. 35, no. 1, pp. 25–28, 2012.

[22] H. Bao, X. L. Pan, and S. Y. Feng, "A fuzzy network method for the airfoil long baseline antenna deformation measurement," in *Fifth Asia International Symposium on Mechatronics (AISM 2015)*, p. 6, Guilin, China, 2015.

[23] S. Xiao, M. Liu, Y. T. Zhijian, and K. Yun, "Study on the deformation measurement of structure based on fiber Bragg grating sensor," *2016 IEEE International Conference on Mechatronics and Automation*, 2016, Harbin, China, 2016.

[24] A. E. Hoerl and R. W. Kennard, "Ridge regression: biased estimation for nonorthogonal problems," *Technometrics A Journal of Stats for the Physical Chemical & Engineering ences*, vol. 42, no. 1, pp. 80–86, 2000.

[25] H. Qunge, X. Chang, and D. Yufan, "Dam deformation analysis based on ridge regression," in *In 2009 International Conference on Information Engineering and Computer Science*, pp. 1–4, Wuhan, China, 2009.

[26] G. C. Cawley and N. L. C. Talbot, "Reduced rank kernel ridge regression," *Neural Processing Letters*, vol. 16, no. 3, pp. 293–302, 2002.

[27] S. Qing, Q. Duoyang, W. Bing, Y. Li, and B. Liu, "DCR and applications based on PSO-SVM algorithm," *China Mechanical Engineering*, vol. 29, no. 15, pp. 1875–1883, 2018.

[28] R. Eberhart and J. Kennedy, "A new optimizer using particle swarm theory," in *Mhs 95 Sixth International Symposium on Micro Machine & Human Science*, pp. 39–43, Piscataway, NJ, USA, 2002.

[29] Y. Shi, "Particle swarm optimization: developments, applications and resources," in *In Proceedings of the 2001 congress on evolutionary computation*, pp. 81–86, Seoul, Korea (South), 2001.

[30] R. Pahlevi, M. A. Murti, and E. Susanto, "The implementation of PID using particle swarm optimization algorithm on networked control system," in *In 2014 International Conference on Industrial Automation, Information and Communications Technology*, pp. 35–38, Bali, Indonesia, 2014.

[31] B. Ziyang and Y. Jizhou, *Intelligent Optimization Algorithm and MATLAB Example*, Publishing House of Electronics Industry, Beijing, China, 2016.

[32] M. Xuan, *Research on the Aero Engine Blade Film Hole Diameter and Position Accuracy Measurement*, Dalian University of Technology, 2018.

[33] H. Tanliang, D. Xiaohong, W. Haihua, W. Shenlong, and X. Shipeng, "Uncertainty analysis for complex test based on PSO-LSSVM," *University of Shanghai for Science and Technology*, vol. 43, no. 1, pp. 29–34, 2021.

[34] Z. Daye, D. Xiaohong, W. Shenlong, W. Haihua, and Y. Huijie, "Uncertainty evaluation method of complex nonlinear system test based on support vector machine model," *Journal of Mechanical Engineering*, vol. 54, no. 8, pp. 177–184, 2018.

[35] W. Chuanda, *Research on Deformation Measurement and Displacement Reconstruction Theory for Wing Based on Strain Information*, Xidian University, 2015.